

Article

Influence of New Parameterization Schemes on Arctic Sea Ice Simulation

Yang Lu ¹ , Xiaochun Wang ^{1,*}, Yijun He ¹ , Jiping Liu ^{2,3}, Jiangbo Jin ⁴, Jian Cao ⁵, Juanxiong He ⁴, Yongqiang Yu ⁴, Xin Gao ⁴, Mirong Song ⁴ and Yiming Zhang ⁴

¹ School of Marine Sciences, Nanjing University of Information Science and Technology, Nanjing 210044, China; 202219000003@nuist.edu.cn (Y.L.); yjhe@nuist.edu.cn (Y.H.)

² School of Atmospheric Sciences, Sun Yat-sen University, Zhuhai 519082, China; liujp63@mail.sysu.edu.cn

³ Southern Marine Science and Engineering Guangdong Laboratory (Zhuhai), Zhuhai 519082, China

⁴ Institute of Atmospheric Physics, Chinese Academy of Sciences, Beijing 100029, China;

jinjiangbo@mail.iap.ac.cn (J.J.); hejx@mail.iap.ac.cn (J.H.); yyq@lasg.iap.ac.cn (Y.Y.);

gaoxin@mail.iap.ac.cn (X.G.); songmirong@lasg.iap.ac.cn (M.S.); ymzhang@mail.iap.ac.cn (Y.Z.)

⁵ School of Atmospheric Sciences, Nanjing University of Information Science and Technology, Nanjing 210044, China; jianc@nuist.edu.cn

* Correspondence: xcwang@nuist.edu.cn

Abstract: Two coupled climate models that participated in the CMIP6 project (Coupled Model Intercomparison Project Phase 6), the Earth System Model of Chinese Academy of Sciences version 2 (CAS-ESM2-0), and the Nanjing University of Information Science and Technology Earth System Model version 3 (NESM3) were assessed in terms of the impact of four new sea ice parameterization schemes. These four new schemes are related to air–ice heat flux, radiation penetration and absorption, melt ponds, and ice–ocean flux, respectively. To evaluate the effectiveness of these schemes, key sea ice variables with and without these new schemes, such as sea ice concentration (SIC) and sea ice thickness (SIT), were compared against observation and reanalysis products from 1980 to 2014. The simulations followed the design of historical experiments within the CMIP6 framework. The results revealed that both models demonstrated improvements in simulating Arctic SIC and SIT when the new parameterization schemes were implemented. The model bias of SIC in some marginal sea ice zones of the Arctic was reduced, especially during March. The SIT was increased and the transpolar gradient of SIT was reproduced. The changes in spatial patterns of SIC and SIT after adding new schemes bear similarities between the two coupled models. This suggests that the new schemes have the potential for broad application in climate models for simulation and future climate scenario projection, especially for those with underestimated SIT.

Keywords: earth system model; sea ice parameterization scheme; arctic sea ice; sea ice concentration; sea ice thickness



Citation: Lu, Y.; Wang, X.; He, Y.; Liu, J.; Jin, J.; Cao, J.; He, J.; Yu, Y.; Gao, X.; Song, M.; et al. Influence of New Parameterization Schemes on Arctic Sea Ice Simulation. *J. Mar. Sci. Eng.* **2024**, *12*, 555. <https://doi.org/10.3390/jmse12040555>

Academic Editor: Anatoly Gusev

Received: 14 February 2024

Revised: 23 March 2024

Accepted: 24 March 2024

Published: 26 March 2024



Copyright: © 2024 by the authors. Licensee MDPI, Basel, Switzerland. This article is an open access article distributed under the terms and conditions of the Creative Commons Attribution (CC BY) license (<https://creativecommons.org/licenses/by/4.0/>).

1. Introduction

The Coupled Model Intercomparison Project Phase 6 (CMIP6) is ongoing under the leadership of the World Climate Research Program (WCRP) Working Group on Coupled Modelling (WGCM) [1]. The evaluation of sea ice simulation is an essential part of CMIP6 [2]. CMIP6 sea ice output has been widely analyzed and it is found that coupled models involved in the comparison still have biases in the simulation of main sea ice variables such as sea ice concentration (SIC), sea ice extent (SIE), and sea ice thickness (SIT) [3–10]. CMIP6-coupled models from China have also been evaluated to identify common issues [4]. It was found that the Chinese CMIP6 models tend to overestimate the March SIC in marginal ice zones, especially in the Pacific region, and underestimate the September SIC in the central Arctic. These results indicate that the sea ice models in climate models from Chinese research institutions still need further improvement.

The Los Alamos Sea Ice Model (CICE) [11] is commonly used in climate models. For the current resolution of climate models, many sub-grid-scale processes have to be parameterized, such as air–sea heat flux, radiation, melt pond, ice–ocean flux, etc. The bulk flux formula [12] uses the difference in temperature and humidity between ice surface and near-surface air and surface winds, together with empirical transfer coefficients to calculate ice surface heat fluxes. However, the empirical coefficients could bring uncertainty in flux calculation. The delta-Eddington (dEdd) scheme [13] is used for shortwave radiation calculation in CICE. It uses the inherent optical properties (IOP) to calculate the apparent optical (AOP) such as albedo and transmittance, which directly links albedo and sea ice characteristics. However, ice microstructures (gas bubbles, brine pockets, and particulate matter) inside the sea ice are not considered. These ice microstructures could have a significant effect on radiation transfer. The Community Earth System Model (CESM) scheme [14], Topography (TOPO) scheme [15], and Level ice (LVL) scheme [16] are three melt pond schemes of CICE. Among them, the LVL scheme is commonly used. The LVL scheme assumes that the melt ponds can only exist on level ice and uses the level ice variable in CICE to carry melt pond tracers. The change in melt pond area and melt pond depth is determined by an empirical parameter pond aspect ratio. The problem with this scheme is that few observations can be used to constrain the pond aspect ratio parameter. Furthermore, the horizontal sizes of melt ponds can have influences on melt pond depth and radiation transfer but these factors are not considered in the LVL scheme. The default ice–ocean heat flux parametrization scheme in CICE is a two-equation (2EQ) scheme [17,18]. One equation describes the energy balance at the ice–ocean interface between the heat conduction within sea ice and oceanic heat flux from below. Another equation calculates the ocean freezing point from mixed-layer salinity. However, the 2EQ scheme could simulate a lower freezing temperature and thinner SIT [19,20].

These four processes are computed by new schemes and tested in two coupled models. The Earth System Model of Chinese Academy of Sciences version 2 (CAS-ESM2-0) [21] and the Nanjing University of Information Science and Technology Earth System Model version 3 (NESM3) [22] are two of the nine Chinese models participating in CMIP6 (Table 1, column 1 and column 3, hereafter referred as CAS-ESM2-0 old version and NESM3 old version). Table 1 presents the details of the configuration of these two coupled models in terms of their atmosphere, ocean, land, sea ice component, and coupler. Since CMIP6, four new sea ice parameterization schemes (Table 2) have been developed and implemented in the above two Chinese models (Table 1, column 2 and column 4, hereafter referred to as CAS-ESM2-0 new version and NESM3 new version). The four schemes are the maximum entropy production (MEP) scheme, the melt pond size distribution (MPSD) scheme, the Inherent optical properties (IOP) scheme, and the three-equation ice–ocean boundary layer (3EQ) scheme. The MEP scheme [23] was originally developed for land surface heat flux calculation and is adapted to use for air–ice heat flux calculation. It uses just radiation heat flux and temperature to compute sensible and latent heat flux directly. The IOP scheme [24] was developed to describe the effects of ice microstructure on inherent optical properties and used with the dEdd scheme to calculate the apparent optical properties of sea ice. The MPSD scheme [25] is used to determine the sub-grid melt pond size distribution after the melt pond fraction is calculated by melt pond schemes such as the LVL scheme. The three-equation (3EQ) scheme [26] uses the salinity of the ice–ocean interface to define the interfacial freezing temperature. An equation describing the salt flux balance at the ice–ocean interface is also added. The summary of four new sea ice schemes can be found in Table 2. Detailed explanations of these sea ice schemes are provided in Appendix A.

The implementation of these four new schemes is expected to improve the sea ice component model and hence the coupled model. Therefore, it is necessary to make a complete evaluation of their influence on global coupled sea ice simulation. In this study, an assessment of the two coupled models with and without new schemes is presented. The remainder of this paper is structured as follows. In Section 2, the coupled climate models, datasets, and comparison methods are introduced. In Section 3, the simulations from the

two coupled models with and without four new schemes are compared. In Section 4, the influence of new schemes is discussed. The conclusion of the present study is summarized in Section 5.

Table 1. Details of the CAS-ESM2-0 model and NESM3 model.

Component	CAS-ESM2-0 Old Version	CAS-ESM2-0 New Version	NESM3 Old Version	NESM3 New Version
Atmosphere	IAP AGCM5	IAP AGCM5	ECHAM6.3	ECHAM6.3
Ocean	LICOM2	LICOM3	NEMO3.4	NEMO3.4
Sea Ice	CICE4	CICE6	CICE4	CICE6
Land	CoLM	CoLM	JSBACH	JSBACH
Coupler	Coupler7	Coupler7	OASIS_3.0-MCT3	OASIS_3.0-MCT3

Table 2. Summary of four old and new sea ice schemes.

Scheme	Air–Ice Heat Flux Exchanges	Shortwave Radiation	Melt Pond	Ice–Ocean Heat Flux Exchanges
old version	Bulk formula	dEdd	LVL	2EQ
new version	MEP	dEdd + IOP	LVL + MPSD	3EQ

2. Materials and Methods

2.1. Model Description

2.1.1. The CAS-ESM2-0 Earth System Model

The CAS-ESM2-0 Earth System Model’s old version consists of four component models, which are coupled together by the CESM Coupler7 [27]. The atmospheric component model of CAS-ESM2-0 is IAP AGCM. The land component model is the Beijing Normal University/IAP Common Land Model (CoLM), with the IAP Vegetation Dynamics Model and IAP fire model embedded. The ocean component model is the LASG/IAP Climate System Ocean Model (LICOM) with the IAP ocean biogeochemistry model embedded. The sea ice component model is CICE. It is based on an ice thickness distribution function with 5 thickness categories [28]. The vertical grid contains four ice layers and one snow layer on top of the ice. Elastic–viscous–plastic rheology [29] and incremental remapping advection schemes are used to describe the geophysical scale motion of sea ice. The horizontal grid spacing is nearly 1 degree. The mechanical redistribution scheme is used to describe the local scale ice motion [30]. Detailed model descriptions of the version participating CMIP6 (old version) can be found in [31,32]. The difference between the new version CAS-ESM2-0 and the old version is the addition of four new parameterization schemes in the updated sea ice component model from v4 to v6 and a change in the ocean model mainly in terms of the tri-polar grid (Tables 1 and 2).

2.1.2. The NESM3 Earth System Model

The NESM3 Earth System Model old version consists of three component models, which are coupled together by the OASIS_3.0-MCT3 coupler [33]. The atmospheric component model of NESM3 is ECHAM6.3, with the JSBACH land surface model embedded [34]. The ocean and sea ice component models are NEMO3.4 [35] and CICE4 [36], respectively. The horizontal resolution of the atmospheric component model is nearly 1.9 degrees. There are 47 vertical levels in the atmospheric model from the surface to 0.01 hPa. The ocean component model uses a tri-polar grid system with a horizontal resolution of nearly 1 degree. There are 46 vertical layers in the ocean model, with 10 layers in the uppermost 100 m. The sea ice component model is configured from CICE4, which uses a displaced-polar grid system with a horizontal resolution of $\sim 1^\circ \times \sim 0.5^\circ$. Detailed model descriptions and model development of the old version can be found in [37]. The new version of NESM3 model in

present research is an update of sea ice component model from v4 to v6 and the addition of four new schemes (Tables 1 and 2).

2.2. Observation Data Used for the Evaluation

2.2.1. NSIDC Sea Ice Concentration

Observational data are essential for understanding the Arctic climate system, sea ice, and assessing sea ice models. However, in situ observations in the Arctic region are highly sparse in time and space, which are not easy to use in model evaluation. Satellites can obtain sea ice observations that are abundant to be compared with model simulations. At present, the commonly used satellite SIC observations are mainly retrieved from passive microwave brightness temperatures. Two retrieval algorithms, the NASA Team (NT) algorithm and Bootstrap (BT) algorithm, are widely used. The algorithms are both mature and well-validated. Inter-comparison of NT and BT algorithms found that the BT algorithm performs better, although they both underestimate the summer SIC [38]. Therefore, in this study, the SIC product from the BT algorithm was selected as the reference data for assessing the simulated SIC. This dataset has a spatial coverage of the entire Arctic and Antarctic region with a resolution of 25 km × 25 km. The time range is from 25 October 1978 to present, with a resolution of one day. It should be mentioned that the SIC may be underestimated due to melt ponds [39,40] or very low temperatures [41].

2.2.2. PIOMAS Sea Ice Thickness

The mostly used satellite SIT observations are monthly averaged Arctic SIT data retrieved from ICESat, ICESat-2, and CryoSat-2 satellite altimetry data [42–44]. However, the retrieval of SIT is still affected by factors such as snow on the ice, melt ponds, and sea ice density. Although satellite altimetry can provide winter SIT data from January to April and October to December, it lacks summer SIT observations from May to September. This has limited the usage of satellite SIT in model evaluation. Recently, new algorithm was developed to retrieve SIT from the reflectivity data of Global Navigation Satellite System-Reflectometry (GNSS-R) [45]. However, the SIT retrieved using GNSS-R has not been fully examined. Therefore, SIT product from the Pan-Arctic Ice Ocean Modeling and Assimilation System (PIOMAS) [46] was used as the reference data to assess the simulated SIT. PIOMAS was developed to assimilate the satellite-observed SIC and sea surface temperature (SST) in a global ice–ocean coupled model. Leap years in PIOMAS are treated by integrating forward for 365 days. The PIOMAS thickness data are provided in the form of averaged thickness over the model grid for regions with ice thicker than 0.15 m. This dataset is widely used for sea ice model validation and evaluation. The time range is from 1978 to present, with a resolution of one month. PIOMAS can capture the major patterns of SIC and SIT in both polar oceans [46]. PIOMAS results are in reasonably good agreement with submarine SIT observations. The SIT biases are within 9% in the Arctic [46].

2.3. Taylor Score

The Taylor Score (TS) [47] was used here to assess the performance of the two models in simulating the spatial pattern of a particular sea ice variable such as SIC or SIT, which is defined as

$$TS = \frac{4(1 + R)^4}{\left(\frac{\sigma_m}{\sigma_o} + \frac{\sigma_o}{\sigma_m}\right)^2 (1 + R_0)^4}, \quad (1)$$

where R is the pattern correlation coefficient of the observations and model outputs and R_0 is the maximum attainable value of R taken as 1 in our study. σ_m is the standard deviation of the model field and σ_o is the standard deviation of the observation field. A higher TS value indicates a greater similarity between the model field and the observation field.

2.4. Data Processing

SIC and SIT are two important physical variables of sea ice. Both NSIDC SIC observation and PIOMAS SIT products started in 1978. Both run with and without new parameterization schemes follow the design of the CMIP6 historical experiment and span from 1850 to 2014. The comparison conducted in this study is from 1980 to 2014. All data have been gridded into $1^\circ \times 1^\circ$ before comparison for convenience. The SIC data have been scaled into 0–1 interval. All grid cells participate in the calculation of SIC and SIT differences and Taylor Score calculation. The SIT from the NESM3 old version is provided in the form of actual sea ice thickness, which is the ice thickness averaged over the ice-covered area of a grid cell. This dataset is converted into equivalent sea ice thickness to match PIOMAS product and CAS-ESM2-0 output by multiplying the SIT of each grid cell by its SIC.

3. Results

3.1. Spatial Patterns of SIC and SIT

Figure 1 compares the climatological (1980–2014) spatial pattern of observed and simulated SIC with and without these four new schemes. After adopting the new parameterization schemes, the simulated March SIC is reduced and is closer to NSIDC data (Figure 1a,c,e) for both models, especially in the Pacific sector. In March, excessive marginal sea ice cover around the Bering Strait and Okhotsk Sea is corrected by applying the new schemes. However, there are still some unrealistic features when these new schemes are used, such as too much sea ice being generated in the Greenland Sea and Barents Sea. In September, the situation of the two models differs. For the CAS-ESM2-0 model, the new version has a more realistic spatial distribution compared with the observation of the old version (Figure 1f–h). For the NESM3 model, the new version has higher SIC in the central Arctic than the old version and is more similar to the observation. However, the NESM3 new version has a much larger spatial coverage of high SIC compared to the old version and is further deviated from the observation (Figure 1f,i,j).

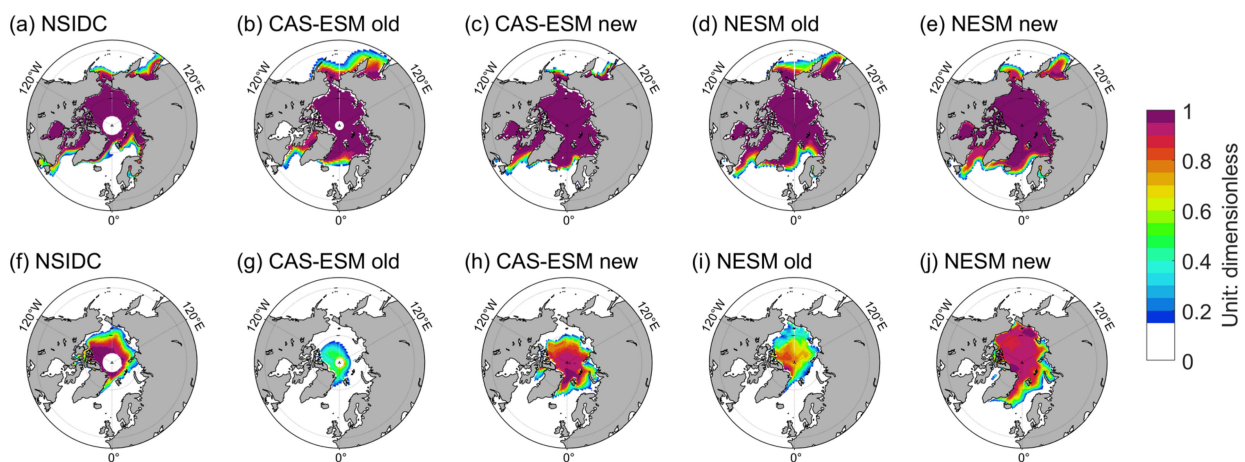


Figure 1. Spatial distribution of climatological (1980–2014) March (upper) and September (lower) SIC from NSIDC observation (a,f), CAS-ESM2-0 old version (b,g), CAS-ESM2-0 new version (c,h), NESM3 old version (d,i), and NESM3 new version (e,j).

After applying the new parameterization schemes, the simulated March and September SIT is increased in both models. Figure 2 compares the climatological (1980–2014) spatial pattern of observed and simulated SIT with and without these four new schemes. The observed SIT reduces gradually from west to east. The thickest ice (thicker than 5 m) is in the west of the Arctic, north of the Canadian Arctic Archipelago. The central Arctic sea ice has a thickness of around 3 m. In the east of the Arctic, the sea ice is much thinner (less than 2 m). Therefore, the PIOMAS March and September SIT has a transpolar gradient

(Figure 2a,f). This gradient has been reproduced in both models with the addition of four new schemes in both March and September (Figure 2c,e,h,j). However, the SIT has been adjusted too much in the Beaufort Sea, Chukchi Sea, and Baffin Bay.

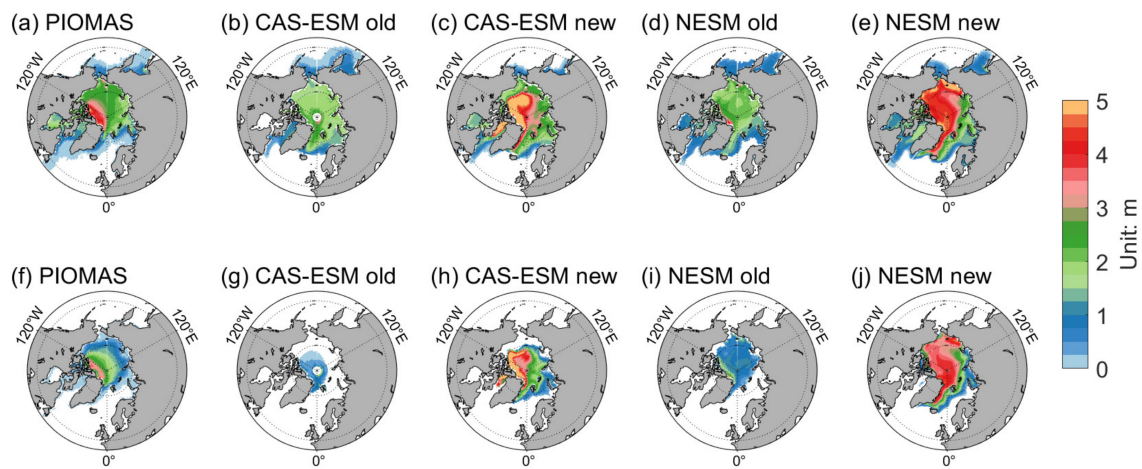


Figure 2. Spatial distribution of climatological (1980–2014) March (upper) and September (lower) SIT from PIOMAS (a,f), CAS-ESM2-0 old version (b,g), CAS-ESM2-0 new version (c,h), NESM3 old version (d,i), and NESM3 new version (e,j).

The difference of SIC with and without new schemes bears similarity between the two models (Figures 3 and 4). Black dots on Figures 3 and 4 represent points that are significant at a 99% confidence level for the Student's *t*-test. Figure 3 shows the multi-year mean monthly SIC difference between the CAS-ESM2-0 new version and the old version from January to December (the result of the new version minus that of the old version). It can be concluded that there are two types of spatial patterns in the SIC difference of CAS-ESM2-0. From December to May, the SIC of the new version decreases in the Pacific and increases in the Atlantic. From June to November, the SIC of the new version increases in the central and marginal Arctic Ocean. Figure 4 shows the monthly SIC difference between the NESM3 new version and the old version from January to December (a result of the new version minus that of the old version). Similar to the situation of CAS-ESM2-0, from December to May, the SIC of the new version decreases in the Pacific and increases in the Atlantic. From June to November, the SIC of the new version increases in the central and marginal Arctic Ocean. Comparing Figures 3 and 4, the differences in SIC from two models with and without four parameterization schemes are very similar in their spatial patterns and temporal evolutions. The results of the *t*-test show that the SIC changes associated with these four new schemes are significant in most regions mentioned above.

The SIT difference of these two coupled models with and without these four new schemes are also similar (Figures 5 and 6). Black dots in Figures 5 and 6 represent points that are significant at a 99% confidence level for the Student's *t*-test. Figure 5 shows the difference of multi-year monthly mean SIT difference between the CAS-ESM2-0 new version and the CAS-ESM2-0 old version. From January to December, positive SIT difference exists in the western part of the Arctic, including Baffin Bay, Beaufort Sea, and Chukchi Sea. This spatial pattern of SIT difference shows minor seasonal variations. Figure 6 shows the difference in multi-year monthly mean SIT between the NESM3 new version and the old version. Though similar to the spatial pattern of the CAS-ESM2-0 SIT difference, a positive SIT difference exists over the entire Arctic for the NESM3 and the magnitude of the SIT difference from the NESM3 is smaller than that of CAS-ESM2-0. Comparing Figures 5 and 6, it could be concluded that the difference in SIT with and without new schemes from the two coupled models is similar in that the SIT increased over the entire Arctic throughout the whole year. The results of the *t*-test show that the SIT differences associated with these four new schemes are significant in most regions.

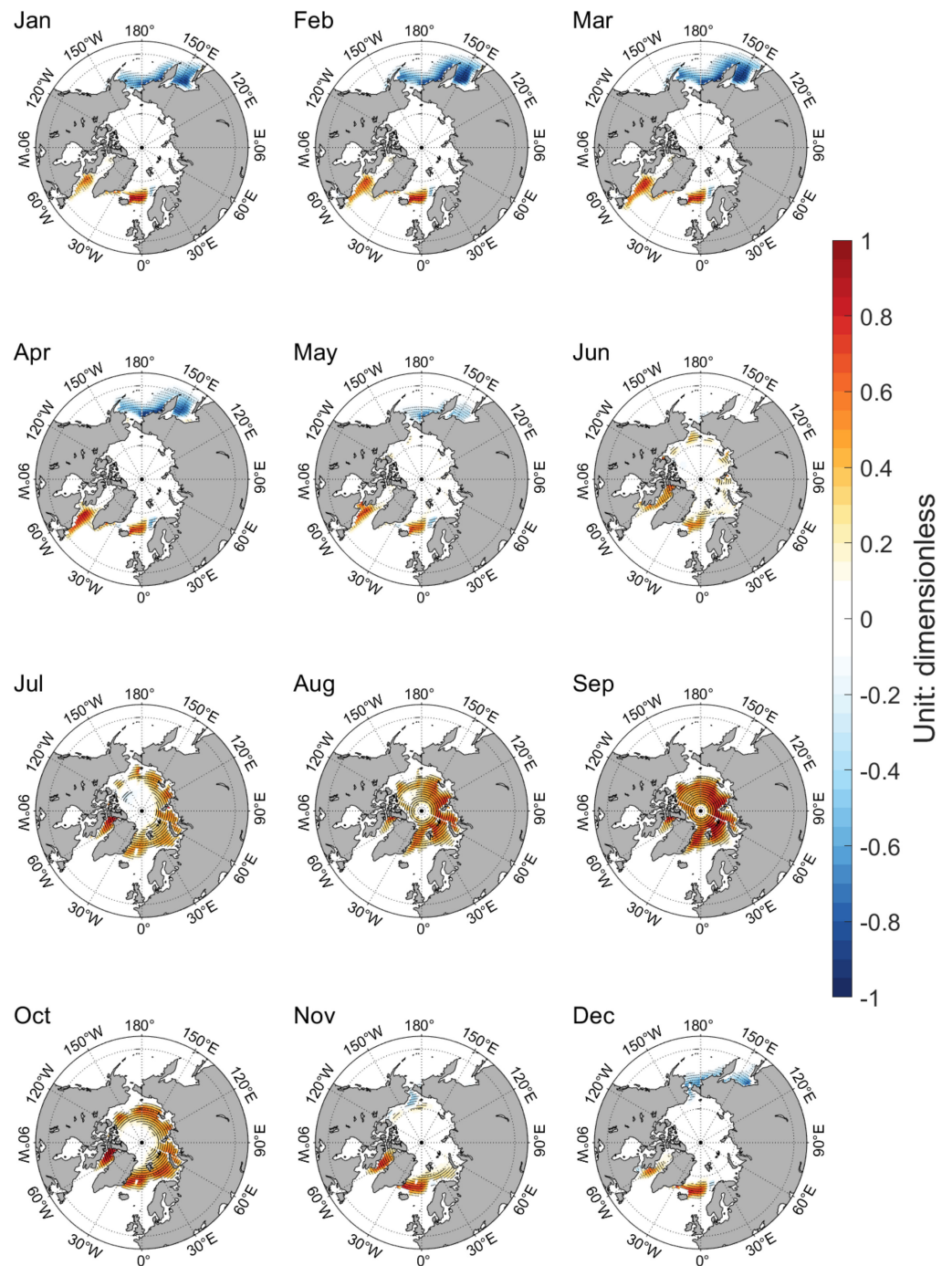


Figure 3. Climatological (1980–2014) monthly evolution of SIC differences between CAS-ESM2-0 new version and old version (new version minus old version). Black dots represent points that are significant at a 99% confidence level for the Student’s *t*-test.

3.2. Taylor Score of the 1980–2014 Mean SIC and SIT

The Taylor Score (TS) provides a quantitative measure when comparing the spatial distribution of two fields. To assess the overall improvement for the entire year, TS was computed between model SIC output and SIC observation, model SIT output, and PIOMAS product. Figure 7 shows the TS value of the 1980–2014 multi-year mean SIC of the old and new versions of the two models from January to December. For the CAS-ESM2-0, the TS value of the old version has its minimum in September (red dashed line). The TS value of the new version (red solid line) is higher than that of the old version, especially in

August and September. For the NESM3 model, the TS value of the old version is around 0.5 without significant seasonal variations (green dashed line) and the TS value of the new version (green solid line) with the addition of four new schemes is about 0.1 higher than that of the old version. With these new schemes, the SIC spatial distribution of the two models is improved over the entire year.

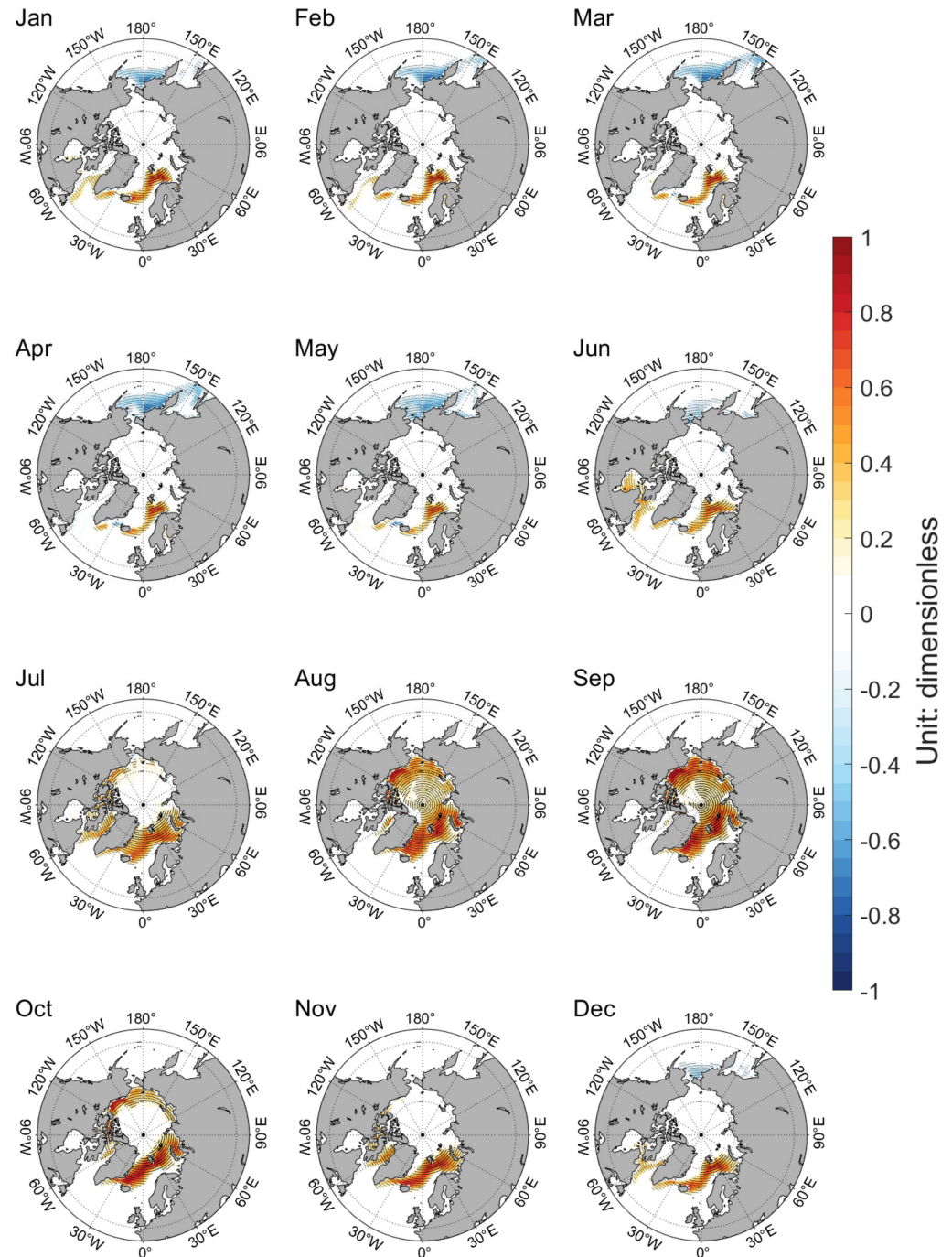


Figure 4. Climatological (1980–2014) monthly evolution of SIC differences between NESM3 new version and old version (new version minus old version). Black dots represent points that are significant at a 99% confidence level for the Student’s *t*-test.

Figure 8 shows the TS value of the 1980–2014 multi-year mean SIT of the old and new versions of the two models by comparing model SIT with the PIOMAS product. For the CAS-ESM2-0 model, the TS value of the old version has its minimum in September (red

dashed line). The TS value of the new version (red solid line) is higher than that of the old version in July, August, September, and October but slightly lower in other months. For the NESM3 model, the TS value of the old version has its minimum in August (green dashed line). The TS value of the new version (green solid line) is higher than that of the old version in July, August, September, and October. With these new schemes, the SIT spatial distribution of the two models is improved in the melting season.

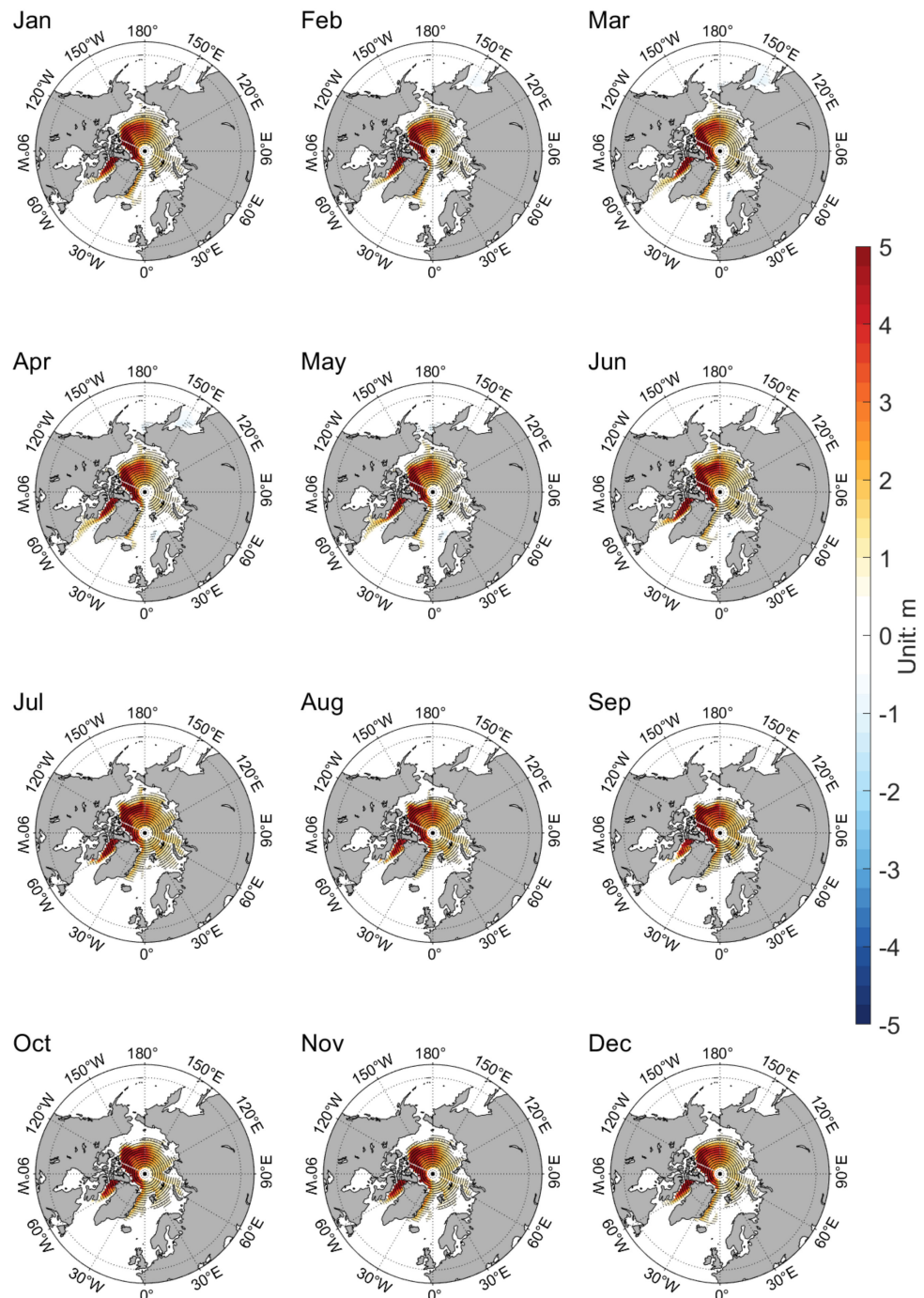


Figure 5. Climatological (1980–2014) monthly of SIT differences between CAS-ESM2-0 new version and old version (new version minus old version). Black dots represent points that are significant at a 99% confidence level for the Student’s *t*-test.

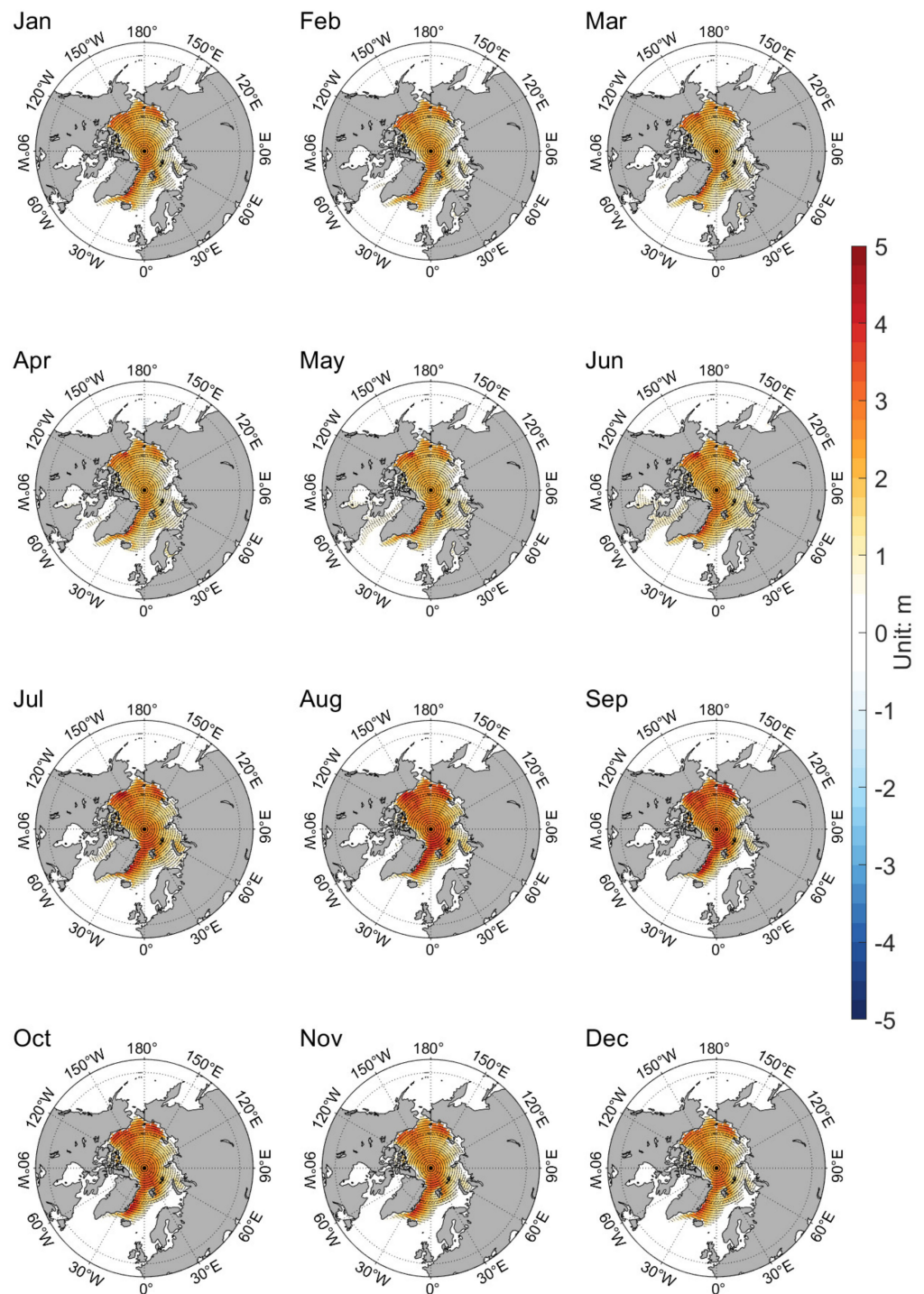


Figure 6. Climatological (1980–2014) monthly of SIT differences between NESM3 new version and old version (new version minus old version). Black dots represent points that are significant for a 99% confidence level for the Student’s *t*-test.

Figures 7 and 8 support the notion that SIC and SIT simulation have been improved in the two coupled models with the addition of four new schemes. The improvement is mainly in the melting season.

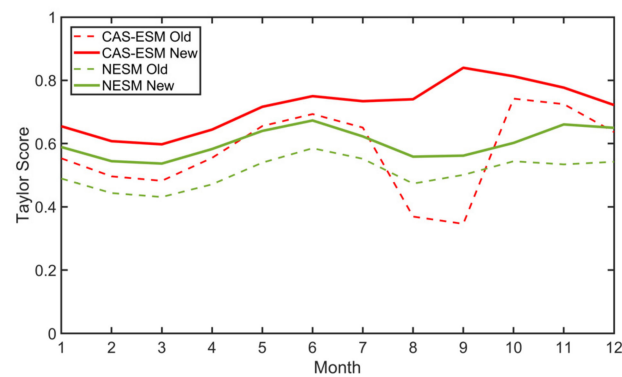


Figure 7. The Taylor Score of the 1980–2014 multi-year mean SIC field from CAS-ESM2-0 old version (red dash line), CAS-ESM2-0 new version (red solid line), NESM3 old version (green dash line), and NESM3 new version (green solid line). All the model SIC fields are compared against the NSIDC observation.

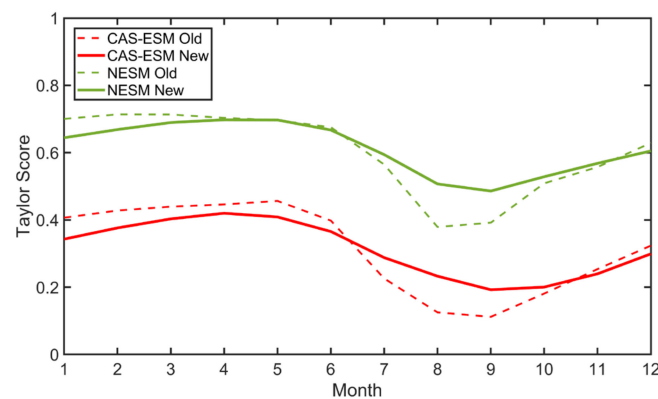


Figure 8. The Taylor Score of the 1980–2014 multi-year mean SIT field from CAS-ESM2-0 old version (red dash line), CAS-ESM2-0 new version (red solid line), NESM3 old version (green dash line), and NESM3 new version (green solid line). All model fields are compared against the PIOMAS product.

4. Discussion

These four new sea ice parameterization schemes mainly influence sea ice thermodynamic processes. In a stand-alone CICE simulation, Zhang et al. compared the MEP scheme with the bulk formula scheme [48]. Their simulation results show that, during sea ice growing season, in the central Arctic, the change in surface heat flux is positive (positive heat flux represents upward heat flux from the sea ice to the atmosphere, while negative heat flux represents downward heat flux from the atmosphere to the sea ice) and ocean tends to lose more heat, and this effect could increase local SIT. Their simulation results also show that, during the melting season, the change in surface heat flux is negative in the central Arctic but positive in the marginal seas. This could lead to an increase in heat loss of marginal sea ice during the melting season, hence increasing SIT. Overall, in Zhang’s stand-alone CICE simulation, for the whole year, the simulated SIT using the MEP scheme is thicker than that of the bulk formula scheme. This is consistent with the coupled simulation in this paper, as is shown in Figure 2.

In stand-alone sea ice model simulations, compared to the 2EQ scheme, the 3EQ parameterization leads to thicker ice [26,49], especially in the marginal ice zone during summer. In these stand-alone simulations, the salinity of the ice–ocean interface in the 3EQ scheme is much lower than the salinity of the ocean mixed layer in the 2EQ scheme. Therefore, the freezing temperature at the ice–ocean interface is relatively higher than that of the 2EQ scheme, hence narrowing the gap between seawater temperature and the freezing temperature at the ice–ocean interface. This reduces the upward temperature gradient

towards the interface, leading to a decrease in oceanic turbulent heat flux. Meanwhile, the downward heat conduction in ice is also decreased due to the reduced temperature gradient between the ice bottom and ice–ocean interface. Finally, the decrease in upward oceanic heat flux and downward heat conduction could decrease the basal melt of sea ice and increase SIT. In this paper, the application of the 3EQ scheme in the two coupled models leads to a thicker summer SIT in the marginal ice zone, as is seen in Figure 2, which is consistent with the previous stand-alone simulations.

Though more numerical simulations and diagnostic analysis are needed to understand the effect of each individual parameterization scheme, the consistency between coupled and stand-alone simulation is reassuring. The Arctic is an amplifier and indicator of global climate change. The projection of the timing of Arctic ice-free summer is a current research topic with great societal impacts. Several researchers pointed out that models with poor simulation skills are likely to reduce the accuracy of multi-model ensemble projection [50,51]. In this study, we found that the four new sea ice parameterization schemes improved the historical simulation of Arctic sea ice. Naturally, these new schemes may improve the historical climate simulation and reduce the projection uncertainty in the timing of Arctic ice-free summer.

5. Conclusions

Four new sea ice parameterization schemes, namely the MEP scheme, IOP scheme, MPSD scheme, and 3EQ scheme, were added into two very different CMIP6 climate models, the CAS-ESM2-0 model and the NESM3 model. These four new schemes are related to the computation of air–ice heat flux, radiation penetration and absorption, melt ponds, ice–ocean heat, and salt fluxes. In this work, an evaluation and comparison of the sea ice variables (sea ice concentration and sea ice thickness) of the two models were carried out based on numerical simulation with and without these four schemes and these simulations follow the CMIP6 historical experiment setup. The main conclusions are as follows.

(1) New parameterization schemes improved SIC and SIT in the Arctic region. The SIC spatial pattern with the new schemes is closer to observation. The March SIC overestimation in the Bering Strait and Okhotsk Sea is reduced. The September SIC underestimation is also reduced. The spatial gradient of SIT from the western Arctic to the eastern Arctic is reproduced in the new version of the two models;

(2) The improvement in modeling SIC and SIT is shown by the similarity of the spatial pattern of these two fields compared with observation and PIOMAS products, as shown by Taylor Scores. With new schemes, the TS values of SIC from two models have been improved by around 0.1 for all months. The TS values of SIT from the two models have been improved by around 0.2 in the melting season;

(3) The changes in spatial pattern of SIC and SIT after adding new schemes share certain common features between the two different coupled models. For the two models, the SIC decreases in the Pacific and increases in the Atlantic in winter and spring season (December to May) and increases over the entire Arctic in summer and autumn season (from June to November). For the two models, the SIT increases over the entire Arctic throughout the entire year.

There should be interactions among these four sea ice schemes and other sea ice parameterization schemes. This increases the difficulty when explaining the combined contribution of these four new schemes in a coupled model. Instead of analyzing their individual effects, the combined effects of these four schemes are investigated in the historical experiment setup of CMIP6. More numerical simulations and diagnostic analysis could be conducted to understand the effect of each individual scheme in the future.

Since CAS-ESM2-0 and NESM3 are very different climate models in terms of their component models, coupler, etc., and may represent the performance of other models in CMIP6, the similarity of model improvement after adding new parameterization schemes indicates that these schemes have the potential to be applied in other climate models. By adding these four new parameterization schemes, the sea ice simulation in other models

might be improved as well and the uncertainty in future climate projection may also be reduced based on the improved models, although the scope of improvements needs to be assessed individually.

Author Contributions: Conceptualization, X.W. and J.L.; Data curation, Y.L., J.J. and J.C.; Formal analysis, Y.L.; Funding acquisition, X.W., Y.H., J.L., J.H., Y.Y., X.G. and M.S.; Investigation, Y.L.; Methodology, Y.L. and X.W.; Project administration, X.W. and Y.H.; Resources, X.W. and Y.H.; Software, J.J. and J.C.; Supervision, X.W. and Y.H.; Validation, Y.L. and X.W.; Visualization, Y.L.; Writing—original draft, Y.L.; Writing—review and editing, X.W., Y.H., J.L., J.J., J.C., M.S. and Y.Z. All authors have read and agreed to the published version of the manuscript.

Funding: This study is supported by the National Natural Science Foundation of China (No. 42376200; No. 42005123; No. 42130608), the National Key R&D Program of China (No. 2018YFA0605900).

Institutional Review Board Statement: Not applicable.

Informed Consent Statement: Not applicable.

Data Availability Statement: Data are partly available in a publicly accessible repository. The NSIDC SIC data presented in this study are openly available in <https://nsidc.org/data/G02202/versions/3> accessed on 14 February 2024. The PIOMAS SIT data presented in this study are openly available in <https://psc.apl.uw.edu/data/> accessed on 14 February 2024. The old version of CAS-ESM2-0 and NESM3 coupled model data presented in this study are openly available in <https://aims2.llnl.gov/> accessed on 14 February 2024.

Conflicts of Interest: The authors declare no conflicts of interest.

Appendix A

A brief description of the parameterizations is provided in this section and the main differences between old and new parameterization schemes are pointed out.

Appendix A.1. Bulk Formula Scheme

The bulk formula parameterization scheme is based on planet boundary layer theory. It uses flux-gradient and exchange coefficients to calculate the fluxes of momentum, sensible heat, and latent heat. Following reference [12], the equations are as follows:

$$H_m = \rho C_d U^2, \tag{A1}$$

$$H_s = \rho c_p C_h U (\theta_s - \theta), \tag{A2}$$

$$H_l = \rho L_v C_q U (q_s - q), \tag{A3}$$

where H_m is the momentum flux, H_s is the sensible heat flux, and H_l is the latent heat flux. ρ is the density of air. U , θ , q are wind speed, potential temperature, and specific humidity at height z , respectively. c_p is specific heat capacity at constant pressure, θ_s is the sea-surface skin temperature, and q_s is the saturated specific humidity at the sea-surface skin temperature. L_v is the latent heat of vaporization of seawater. C_d , C_h , and C_q are exchange coefficients depending on height, stability, and roughness length, given by the Monin–Obukhov similarity theory as

$$C_d = \left[\frac{\kappa}{\ln(z/z_{om}) - \psi_m} \right]^2, \tag{A4}$$

$$C_h = \left[\frac{\kappa}{\ln(z/z_{om}) - \psi_m} \right] \left[\frac{\kappa}{\ln(z/z_{oh}) - \psi_h} \right], \tag{A5}$$

$$C_q = \left[\frac{\kappa}{\ln(z/z_{om}) - \psi_m} \right] \left[\frac{\kappa}{\ln(z/z_{oq}) - \psi_q} \right], \tag{A6}$$

where $\kappa = 0.4$ is the von Karmen constant, ψ_m , ψ_h , and ψ_q are the stability functions and z_{om} , z_{oh} , and z_{oq} are the roughness lengths corresponding to transport of momentum, heat, and moisture, respectively. The stability functions are calculated as

$$\psi_m(\zeta) = 2 \ln\left(\frac{1+x}{2}\right) + \ln\left(\frac{1+x^2}{2}\right) - 2 \tan^{-1}(x) + \pi/2; \zeta < 0, \tag{A7}$$

$$\psi_m(\zeta) = -a_2\zeta; \zeta > 0, \tag{A8}$$

$$\psi_h(\zeta) = \psi_q(\zeta) = 2 \ln\left(\frac{1+x^2}{2}\right); \zeta < 0, \tag{A9}$$

$$\psi_h(\zeta) = \psi_q(\zeta) = \psi_m; \zeta > 0, \tag{A10}$$

where $x = (1 - a_1\zeta)^{1/4}$, $a_1 = 16$, $a_2 = 5$, and $\zeta \equiv z/L$ is the stability parameter, while L is the Obukhov length scale defined as

$$L \equiv \frac{-u_*^3\theta_v}{\kappa g(\overline{w'\theta'} + 0.61\overline{w'q'})}, \tag{A11}$$

where u_* is the friction velocity, θ_v is the virtual potential temperature, g is the gravitational acceleration, w' is the turbulence fluctuation of vertical velocity, θ' is the turbulence fluctuation of potential temperature, and q' is the turbulence fluctuation of specific humidity. The roughness length for momentum transport is defined as

$$z_{om} = \alpha u_*^2/g + 0.11\nu/u_*. \tag{A12}$$

The roughness lengths for heat and moisture transport are defined as functions (f and g) of the dimensionless roughness Reynolds number $R_r \equiv (z_{om}u_*/\nu)$:

$$z_{oh} = f(R_r)\nu/u_*, \tag{A13}$$

$$z_{oq} = g(R_r)\nu/u_*, \tag{A14}$$

where α is the Charnock coefficient (typically $\alpha = 0.011$) and ν is the kinematic viscosity of dry air.

Appendix A.2. Maximum Entropy Production (MEP) Scheme

This scheme is based on energy balance over the Earth’s surface. An analytical solution of sensible, latent, and conductive heat fluxes at the surface of sea ice is derived as a function of net shortwave and longwave radiative fluxes and temperature at sea ice surface. Following reference [23], the dissipation function (D) is defined in the MEP model as the function of sensible heat flux H_s , latent heat flux H_l , and conductive heat flux H_c as follows:

$$D(H_s, H_l, H_c) = \frac{2H_s^2}{I_s} + \frac{2H_l^2}{I_l} + \frac{2(Q_{net} + H_c)^2}{I_c}, \tag{A15}$$

where I_s , I_l , and I_c are the thermal inertia for turbulent sensible, latent, and conductive heat fluxes at the ice surface, respectively. Q_{net} is the net radiative flux which is the sum of net shortwave and longwave radiative fluxes. I_c is set to $1.5 \times 10^3 \text{ J m}^{-2} \text{ K}^{-1} \text{ s}^{-1/2}$ for still liquid water, $2.0 \times 10^3 \text{ J m}^{-2} \text{ K}^{-1} \text{ s}^{-1/2}$ for ice, and $469 \text{ J m}^{-2} \text{ K}^{-1} \text{ s}^{-1/2}$ for snow. I_s and I_l are formulated based on the Monin–Obukhov similarity theory:

$$I_0 = \rho c_p \sqrt{C_1 \kappa z} \left(C_2 \frac{\kappa z g}{\rho c_p T_r} \right)^{\frac{1}{6}}, \tag{A16}$$

$$I_s = \rho c_p \sqrt{C_1 \kappa z} \left(C_2 \frac{\kappa z g}{\rho c_p T_r} \right)^{\frac{1}{6}} |H_s|^{\frac{1}{6}} \equiv I_0 |H_s|^{\frac{1}{6}}, \tag{A17}$$

$$I_1 = \sigma I_s, \tag{A18}$$

where ρ is air density, c_p is air specific heat at constant pressure, g is gravitational acceleration, κ is von Karman constant, C_1 and C_2 are two empirical constants, z is the reference height above surface, and $T_r \sim 300K$ is a reference temperature. Assuming that water vapor right above the water–snow–ice surface is in equilibrium with the liquid/solid water, σ is given by

$$\sigma = \sqrt{\alpha} \frac{\Delta}{\gamma}, \tag{A19}$$

where Δ is the slope of the saturation water vapor pressure curve at the surface temperature T_s according to the Clausius–Clapeyron equation, γ is the psychrometric constant, and α is the ratio of eddy diffusivity of turbulent transport of water vapor to that of heat. By minimizing the above dissipation function under the constraint of surface energy balance, the solution of H_s , H_l , and H_c can be derived as the following equations:

$$\left(1 + F(\theta) + \frac{F(\theta)}{\theta} \frac{I_c}{I_0} |H_s|^{-\frac{1}{6}}\right) H_s = Q_{net}, \tag{A20}$$

$$H_l = F(\theta) H_s, \tag{A21}$$

$$F(\theta) = 6 \left(\sqrt{1 + \frac{11}{36} \theta} - 1 \right), \tag{A22}$$

$$\theta(T_s, q_s) = \frac{L_v^2}{c_p R_v} \frac{q_s}{T_s^2}, \tag{A23}$$

where T_s is surface temperature and q_s the surface specific humidity, θ is a parameter characterizing the phase-change, L_v is vaporization heat, and R_v is the gas constant.

Appendix A.3. Delta-Eddington (dEdd) Scheme

For direct radiation at cosine zenith angle μ_{0n} incident on a layer of thickness z and inherent optical properties (IOPs) of scattering coefficient σ , absorption coefficient κ , and single particle scattering asymmetry parameter g , the Delta-Eddington solution for a single layer are given by the following equations [13]:

$$k = \kappa + \sigma, \tag{A24}$$

$$\omega = \sigma / (\kappa + \sigma), \tag{A25}$$

$$f = g^2, \tag{A26}$$

$$\tau = kz, \tag{A27}$$

$$\tau^* = (1 - \omega f) \tau, \tag{A28}$$

$$\omega^* = \frac{(1 - f) \omega}{1 - \omega f}, \tag{A29}$$

$$g^* = \frac{g - f}{1 - f}, \tag{A30}$$

$$\lambda = \sqrt{3(1 - \omega^*)(1 - \omega^* g^*)}, \tag{A31}$$

$$\alpha = \frac{3}{4} \omega^* \mu_{0n} \left(\frac{1 + g^*(1 - \omega^*)}{1 - \lambda^2 \mu_{0n}^2} \right), \tag{A32}$$

$$\gamma = \frac{1}{2} \omega^* \left(\frac{1 + 3g^*(1 - \omega^*) \mu_{0n}^2}{1 - \lambda^2 \mu_{0n}^2} \right), \tag{A33}$$

$$u = \frac{3}{2} \left(\frac{1 - \omega^* g^*}{\lambda} \right), \tag{A34}$$

$$N = (u + 1)^2 e^{\lambda \tau^*} - (u - 1)^2 e^{-\lambda \tau^*}, \tag{A35}$$

$$R(\mu_{0n}) = (\alpha - \gamma)(4u/N)e^{-\tau_0^*/\mu_{0n}} + (\alpha + \gamma)(u + 1)(u - 1) \left[e^{+\lambda \tau_0^*} - e^{-\lambda \tau_0^*} \right] / N - (\alpha - \gamma), \tag{A36}$$

$$T(\mu_{0n}) = (\alpha + \gamma)(4u/N) + (\alpha - \gamma) \left[\frac{(u+1)(u-1)(e^{+\lambda \tau_0^*} - e^{-\lambda \tau_0^*})}{N} \right] e^{-\tau_0^*/\mu_{0n}} - (\alpha + \gamma - 1)e^{-\tau_0^*/\mu_{0n}}, \tag{A37}$$

$$\bar{R} = 2 \int_0^{+1} \mu R(\mu) d\mu, \tag{A38}$$

$$\bar{T} = 2 \int_0^{+1} \mu T(\mu) d\mu, \tag{A39}$$

where $R(\mu_{0n})$ and $T(\mu_{0n})$ are the layer reflectivity and transmissivity to direct radiation, respectively. \bar{R} and \bar{T} are the layer reflectivity and transmissivity to diffuse radiation, respectively. μ is cosine zenith angle. These reflectivities and transmissivities account for multiple scattering within the layer. The solution for multiple scattering between layers is obtained by combining of layers. Then, the apparent optical properties (AOPs) of albedo, absorbed, and transmitted flux can be evaluated.

Appendix A.4. Inherent Optical Properties (IOP) Scheme

Compared to the dEdd scheme, which uses constant sea ice IOPs, this new IOP scheme considers the linkage between ice microstructure and ice optical properties [24]. The basic assumptions are that pure ice can absorb light, whereas gas bubbles can only scatter light and that brine pockets and particulate matter (PM) can both scatter and absorb light. Therefore, the sea ice IOPs, namely bulk scattering coefficient σ , absorption coefficient κ , and single particle scattering asymmetry parameter g can be obtained by the sum of the coefficients of each component, as follows:

$$\sigma = \sigma_b + \sigma_a + \sigma_p = \int_{l_{\min}}^{l_{\max}} \pi r_b^2 Q_b^{\text{sca}} N_b(l) dl + \int_{r_{\min}}^{r_{\max}} \pi r_a^2 Q_a^{\text{sca}} N_a(r) dr + \pi r_p^2 Q_p^{\text{sca}} N_p, \tag{A40}$$

$$\kappa = \kappa_i + \kappa_b + \kappa_p = \kappa_i V_i + \int_{l_{\min}}^{l_{\max}} \pi r_b^2 Q_b^{\text{abs}} N_b(l) dl + \pi r_p^2 Q_p^{\text{abs}} N_p, \tag{A41}$$

$$g = \frac{g_a \sigma_a + g_b \sigma_b + g_p \sigma_p}{\sigma}, \tag{A42}$$

where subscripts i, b, a, and p represent pure ice, brine pockets, gas bubbles, and PM, respectively. k_i is the absorption coefficient of bubble-free ice, V_i is the volume fraction of pure ice, r is the radius of each inclusion, l is the length of each brine pocket, and Q^{sca} and Q^{abs} are the scattering efficiency and absorption efficiency, respectively, which can be calculated through the refractive indices and size of inclusions by Mie theory and N is the size distribution function. The asymmetry coefficients g_a and g_b are set as constants and g_p can be obtained using Mie theory.

Appendix A.5. Level Ice (LVL) Scheme

Following [16], melt water may be produced on a given ice thickness category by melting snow and the surface of the ice. Some of this melt water volume may run off into the ocean and the remainder, $\Delta V_{\text{melt},t}$, is added to the melt pond volume for each time step:

$$\Delta V_{\text{melt}} = r(\rho_i |\Delta h_i| + \rho_s |\Delta h_s| + F_{\text{rain}} \Delta t) a_i, \tag{A43}$$

where ρ_i and ρ_s are the ice and snow densities, $|\Delta h_i|$ and $|\Delta h_s|$ are the thicknesses of ice and snow that melted, F_{rain} is the rainfall rate, Δt is the length of time step, and a_i is the ice area fraction. $r = r_{\text{min}} + (1 - r_{\text{min}})a_i$ is the fraction of the total melt water available that is added to the melt ponds. The parameter r_{min} is the minimum volume fraction of melt water that remains on the ice for small ice area fraction. The growth of fresh pond ice lid is governed by a Stefan approximation equation. The drainage of pond water is simulated using Darcy's law. Pond volume changes ΔV_{pond} are distributed as changes to the area of the ponds a_p and to the depth of the ponds h_p using an assumed aspect ratio parameter $\delta_p = \Delta h_p / \Delta a_p$, which was derived by fitting SHEBA observation data.

$$\Delta V_{\text{melt}} = \Delta V_{\text{pond}} = \Delta h_p \Delta a_p = \delta_p \Delta a_p^2 = \Delta h_p^2 / \delta_p. \tag{A44}$$

Appendix A.6. Melt Pond Size Distribution (MPSD) Scheme

According to observations, the melt pond size distribution is approximated using the following equation [25]:

$$P(r) = \left(\frac{1}{r_0}\right) e^{-\frac{r}{r_0}}, \tag{A45}$$

where r_0 is the mean melt pond radius and r is the radius of a random melt pond. The cumulative density function of r can be derived as

$$C(r) = 1 - e^{-\frac{r}{r_0}}, \tag{A46}$$

which represents the existence probability of melt ponds with a radius that falls within the interval $(-\infty, r)$. Therefore, the existence probability of melt ponds with a radius that falls within the interval (r_{m-1}, r_m) is

$$P_m = \frac{C(r_m) - C(r_{m-1})}{\sum C(r_m) - C(r_{m-1})}. \tag{A47}$$

In current melt pond schemes, the grid mean melt pond fraction a_p and grid mean melt pond depth h_p are calculated as

$$a_p = \sum a_{p,n} a_n, \tag{A48}$$

$$h_p = \sum h_{p,n} a_{p,n}, \tag{A49}$$

where $a_{p,n}$ and $h_{p,n}$ are the mean melt pond fraction and melt pond depth of each ice thickness category n , respectively. a_n is the sea ice concentration of each ice thickness category. Using P_m of each melt pond radius r_m , we can divide $a_{p,n}$ and $h_{p,n}$ into melt ponds groups with different radii:

$$a_{p,n,m} = P_m a_{p,n}. \tag{A50}$$

The depth of these divided melt ponds groups, $h_{p,n,m}$, is obtained by assuming that the rate of increase in pond depth decreases exponentially with pond size as follows:

$$h_{p,n,m} = \alpha_m h_{p,n,1}, \tag{A51}$$

$$\alpha_m = 1 + F_m, \tag{A52}$$

$$F_m = 1 - \exp\left(-\frac{r_m}{r_1}\right), \tag{A53}$$

$$h_{p,n,1} = \frac{h_{p,n}}{\sum \alpha_m P_m}. \tag{A54}$$

The MPSD scheme is applied after mean melt pond fraction and depth are calculated by LVL melt pond scheme. The mean pond will be divided into many small ponds and the pond depth may increase.

Appendix A.7. Two-Equation (2EQ) Scheme

The 2EQ and 3EQ schemes are introduced in [49]. In the 2EQ scheme, the energy balance at the ice–ocean interface is given by the following equation:

$$\rho_i L \dot{h}(t) = f_{\text{condbot}} - \rho_w c_w \alpha_t u_* (T_{\text{fio}} - T_{\text{mix}}), \tag{A55}$$

where ρ_i is the density of sea ice, L is the latent heat of fusion, and $\dot{h}(t) \equiv \partial h / \partial t$ is the rate of growth or ablation in m s^{-1} . f_{condbot} is the heat conduction, ρ_w is the density of seawater, c_w is the specific heat capacity of liquid water, α_t is the turbulent heat transfer coefficient, and u_* is the friction velocity. T_{fio} and T_{mix} are the freezing temperature of seawater at the ice–ocean interface and the temperature of ocean mixed layer, respectively. T_{fio} is taken as a linear function of the ocean mixed layer salinity as follows:

$$T_{\text{fio}} = -\mu S_{\text{mix}}, \tag{A56}$$

where $\mu = 0.054$ is an empirical coefficient for salinity and ocean freezing temperature and S_{mix} is the salinity of the ocean mixed layer.

Appendix A.8. Three-Equation (3EQ) Scheme

In the 3EQ scheme, the energy balance at the ice–ocean interface is given by the following equation:

$$\rho_i \dot{h}(t) \Delta E' = f_{\text{condbot}} - \rho_w c_w \alpha_t u_* (T_{\text{fio}} - T_{\text{mix}}), \tag{A57}$$

$$\Delta E' = E'_0(T_{\text{fio}}, S_{\text{io}}) - E'_i(T_{\text{ib}}, S_{\text{ib}}), \tag{A58}$$

where ρ_i is the density of sea ice, $\dot{h}(t) \equiv \partial h / \partial t$ is the rate of growth or ablation in m s^{-1} , E'_0 is the energy of the seawater, and E'_i is the internal energy of sea ice. T_{fio} and S_{io} are the freezing temperature and salinity of seawater at the ice–ocean interface, respectively. T_{ib} and S_{ib} are the temperature and salinity of the specific volume (of melt water ($\dot{h} > 0$) or new ice ($\dot{h} < 0$)) being transferred at the ice–ocean interface, respectively. T_{fio} and S_{io} are calculated using the following equations:

$$T_{\text{fio}} = -\mu S_{\text{io}}. \tag{A59}$$

To solve for S_{io} , an equation describing the salt flux balance at the ice–ocean interface is added to the 2EQ scheme:

$$(S_{\text{io}} - S_{\text{ib}}) \dot{h}(t) = \alpha_s u_* (S_{\text{mix}} - S_{\text{io}}), \tag{A60}$$

where α_s is the turbulent salt transfer coefficient and u_* is the friction velocity.

The values of T_{ib} and S_{ib} depend on ice melt ($\dot{h} > 0$) or new ice formation ($\dot{h} < 0$) as follows:

$$\begin{cases} S_{\text{ib}} = S_i, (\dot{h} > 0), \\ T_{\text{ib}} = T_i, \end{cases} \text{ or } \begin{cases} S_{\text{ib}} = f_s S_{\text{io}}, (\dot{h} < 0), \\ T_{\text{ib}} = T_{\text{fio}}, \end{cases} \tag{A61}$$

where T_i and S_i are the temperature and salinity of bottom ice and f_s is the fraction of the salinity initially retained within the ice when new ice formed.

References

1. Eyring, V.; Bony, S.; Meehl, G.A.; Senior, C.A.; Stevens, B.; Stouffer, R.J.; Taylor, K.E. Overview of the Coupled Model Intercomparison Project Phase 6 (CMIP6) experimental design and organization. *Geosci. Model Dev.* **2016**, *9*, 1937–1958. [[CrossRef](#)]
2. Notz, D.; Jahn, A.; Holland, M.; Hunke, E.; Massonnet, F.; Stroeve, J.; Tremblay, B.; Vancoppenolle, M. The CMIP6 Sea-Ice Model Intercomparison Project (SIMIP): Understanding sea ice through climate-model simulations. *Geosci. Model Dev.* **2016**, *9*, 3427–3446. [[CrossRef](#)]
3. Chen, L.; Wu, R.; Shu, Q.; Min, C.; Yang, Q.; Han, B. The Arctic Sea Ice Thickness Change in CMIP6's Historical Simulations. *Adv. Atmos. Sci.* **2023**, *40*, 2331–2343. [[CrossRef](#)]
4. Li, J.; Wang, X.; Wang, Z.; Zhao, L.; Wang, J. Evaluation of Arctic sea ice simulation of CMIP6 models from China. *Adv. Polar Sci.* **2022**, *33*, 220–234. [[CrossRef](#)]
5. Watts, M.; Maslowski, W.; Lee, Y.J.; Kinney, J.C.; Osinski, R. A Spatial Evaluation of Arctic Sea Ice and Regional Limitations in CMIP6 Historical Simulations. *J. Clim.* **2021**, *34*, 6399–6420. [[CrossRef](#)]
6. Shen, Z.; Duan, A.; Li, D.; Li, J. Assessment and Ranking of Climate Models in Arctic Sea Ice Cover Simulation: From CMIP5 to CMIP6. *J. Clim.* **2021**, *34*, 3609–3627. [[CrossRef](#)]
7. Long, M.; Zhang, L.; Hu, S.; Qian, S. Multi-Aspect Assessment of CMIP6 Models for Arctic Sea Ice Simulation. *J. Clim.* **2021**, *34*, 1515–1529. [[CrossRef](#)]
8. Shu, Q.; Wang, Q.; Song, Z.; Qiao, F.; Zhao, J.; Chu, M.; Li, X. Assessment of Sea Ice Extent in CMIP6 With Comparison to Observations and CMIP5. *Geophys. Res. Lett.* **2020**, *47*, e87965. [[CrossRef](#)]
9. Roach, L.A.; Dörr, J.; Holmes, C.R.; Massonnet, F.; Blockley, E.W.; Notz, D.; Rackow, T.; Raphael, M.N.; O'Farrell, S.P.; Bailey, D.A.; et al. Antarctic Sea Ice Area in CMIP6. *Geophys. Res. Lett.* **2020**, *47*, e2019GL086729. [[CrossRef](#)]
10. Notz, D.; Community, S. Arctic Sea Ice in CMIP6. *Geophys. Res. Lett.* **2020**, *47*, e2019GL086749. [[CrossRef](#)]
11. Hunke, E.; Allard, R.; Bailey, D.; Blain, P.; Craig, A.; Damsgaard, A.; DuVivier, A.; Grumbine, R.; Hebert, D.; Holland, M.; et al. *CICE-Consortium/CICE: CICE Version 6.0.0*; Los Alamos National Laboratory: Los Alamos, NM, USA, 2018. [[CrossRef](#)]
12. Kauffman, B.G.; Large, W.G. *The CCSM Coupler. Version 5.0.1: Combined User's Guide, Source code Reference, and Scientific Description*; National Center for Atmospheric Research: Boulder, CO, USA, 2002; pp. 1–46.
13. Briegleb, B.P.; Light, B. *A Delta-Eddington Multiple Scattering Parameterization for Solar Radiation in the Sea Ice Component of the Community Climate System Model (No. NCAR/TN-472+STR)*; University Corporation for Atmospheric Research: Boulder, CO, USA, 2007; 100p. [[CrossRef](#)]
14. Holland, M.M.; Bailey, D.A.; Briegleb, B.P.; Light, B.; Hunke, E. Improved Sea Ice Shortwave Radiation Physics in CCSM4: The Impact of Melt Ponds and Aerosols on Arctic Sea Ice. *J. Clim.* **2011**, *25*, 1413–1430. [[CrossRef](#)]
15. Flocco, D.; Feltham, D.L.; Turner, A.K. Incorporation of a physically based melt pond scheme into the sea ice component of a climate model. *J. Geophys. Res. Ocean.* **2010**, *115*, C08012. [[CrossRef](#)]
16. Hunke, E.C.; Hebert, D.A.; Lecomte, O. Level-ice melt ponds in the Los Alamos sea ice model, CICE. *Ocean Model.* **2013**, *71*, 26–42. [[CrossRef](#)]
17. McPhee, M.G. Turbulent heat flux in the upper ocean under sea ice. *J. Geophys. Res. Ocean.* **1992**, *97*, 5365–5379. [[CrossRef](#)]
18. Maykut, G.A.; McPhee, M.G. Solar heating of the Arctic mixed layer. *J. Geophys. Res. Ocean.* **1995**, *100*, 24691–24703. [[CrossRef](#)]
19. Notz, D.; McPhee, M.G.; Worster, M.G.; Maykut, G.A.; Schlu"nzen, K.H.; Eicken, H. Impact of underwater-ice evolution on Arctic summer sea ice. *J. Geophys. Res.* **2003**, *108*, 3223. [[CrossRef](#)]
20. McPhee, M.G.; Morison, J.H.; Nilsen, F. Revisiting heat and salt exchange at the ice-ocean interface: Ocean flux and modeling considerations. *J. Geophys. Res. Ocean.* **2008**, *113*, C06014. [[CrossRef](#)]
21. Zhang, H.; Zhang, M.; Jin, J.; Fei, K.; Ji, D.; Wu, C.; Zhu, J.; He, J.; Chai, Z.; Xie, J.; et al. Description and Climate Simulation Performance of CAS-ESM Version 2. *J. Adv. Model. Earth. Syst.* **2020**, *12*, e2020MS002210. [[CrossRef](#)]
22. Cao, J.; Ma, L.; Liu, F.; Chai, J.; Zhao, H.; He, Q.; Wang, B.; Bao, Y.; Li, J.; Yang, Y.; et al. NUIST ESM v3 Data Submission to CMIP6. *Adv. Atmos. Sci.* **2021**, *38*, 268–284. [[CrossRef](#)]
23. Wang, J.; Bras, R.L.; Nieves, V.; Deng, Y. A model of energy budgets over water, snow, and ice surfaces. *J. Geophys. Res. Atmos.* **2014**, *119*, 6034–6051. [[CrossRef](#)]
24. Yu, M.; Lu, P.; Cheng, B.; Leppäranta, M.; Li, Z. Impact of Microstructure on Solar Radiation Transfer within Sea Ice During Summer in the Arctic: A Model Sensitivity Study. *Front. Mar. Sci.* **2022**, *9*, 861994. [[CrossRef](#)]
25. Popović, P.; Cael, B.B.; Silber, M.; Abbot, D.S. Simple Rules Govern the Patterns of Arctic Sea Ice Melt Ponds. *Phys. Rev. Lett.* **2018**, *120*, 148701. [[CrossRef](#)] [[PubMed](#)]
26. Shi, X.; Notz, D.; Liu, J.; Yang, H.; Lohmann, G. Sensitivity of Northern Hemisphere climate to ice–ocean interface heat flux parameterizations. *Geosci. Model Dev.* **2021**, *14*, 4891–4908. [[CrossRef](#)]
27. Craig, A.P.; Verstein, M.; Jacob, R. A new flexible coupler for earth system modeling developed for CCSM4 and CESM1. *Int. J. High. Perform. Comput. Appl.* **2012**, *26*, 31–42. [[CrossRef](#)]
28. Thorndike, A.S.; Rothrock, D.A.; Maykut, G.A.; Colony, R. The thickness distribution of sea ice. *J. Geophys. Res.* **1975**, *80*, 4501–4513. [[CrossRef](#)]
29. Hunke, E.C.; Dukowicz, J.K. An Elastic Viscous Plastic Model for Sea Ice Dynamics. *J. Phys. Oceanogr.* **1997**, *27*, 1849–1867. [[CrossRef](#)]

30. Lipscomb, W.H.; Hunke, E.C.; Maslowski, W.; Jakacki, J. Ridging, strength, and stability in high-resolution sea ice models. *J. Geophys. Res. Ocean.* **2007**, *112*, C03S91. [[CrossRef](#)]
31. Dong, X.; Jin, J.; Liu, H.; Zhang, H.; Zhang, M.; Lin, P.; Zeng, Q.; Zhou, G.; Yu, Y.; Song, M.; et al. CAS-ESM2.0 Model Datasets for the CMIP6 Ocean Model Intercomparison Project Phase 1 (OMIP1). *Adv. Atmos. Sci.* **2021**, *38*, 307–316. [[CrossRef](#)]
32. Guo, Y.; Yu, Y.; Lin, P.; Liu, H.; He, B.; Bao, Q.; Zhao, S.; Wang, X. Overview of the CMIP6 Historical Experiment Datasets with the Climate System Model CAS FGOALS-f3-L. *Adv. Atmos. Sci.* **2020**, *37*, 1057–1066. [[CrossRef](#)]
33. Valcke, S.; Craig, T.; Coquart, L. *OASIS3-MCT User Guide, OASIS3-MCT 3.0*; CERFACS Technical Report, CERFACS TR/CMGC/15/38; CERFACS: Toulouse, France, 2015.
34. Giorgetta, M.A.; Roeckner, E.; Mauritsen, T.; Bader, J.; Crueger, T.; Esch, M.; Rast, S.; Kornblueh, L.; Schmidt, H.; Kinne, S.; et al. *The Atmospheric General Circulation Model ECHAM6: Model Description*; Max Planck Institute for Meteorology: Hamburg, Germany, 2013; 135p.
35. Gurvan, M.; Bourdallé-Badie, R.; Bouttier, P.-A.; Bricaud, C.; Bruciaferri, D.; Calvert, D.; Chanut, J.; Clementi, E.; Coward, A.; Delrosso, D.; et al. *NEMO Ocean Engine*; Note du pole de modélisation de l'Institut Pierre-Simon Laplace. No 27; Institut Pierre-Simon Laplace (IPSL): Guyancourt, France, 2017. [[CrossRef](#)]
36. Hunke, E.C.; Lipscomb, W.H. *CICE: The Los Alamos Sea Ice Model Documentation and Software User's Manual Version 4.0*; Los Alamos National Laboratory: Los Alamos, NM, USA, 2010.
37. Cao, J.; Wang, B.; Yang, Y.-M.; Ma, L.; Li, J.; Sun, B.; Bao, Y.; He, J.; Zhou, X.; Wu, L. The NUIST Earth System Model (NESM) version 3: Description and preliminary evaluation. *Geosci. Model Dev.* **2018**, *11*, 2975–2993. [[CrossRef](#)]
38. Meier, W.N.; Peng, G.; Scott, D.J.; Savoie, M.H. Verification of a new NOAA/NSIDC passive microwave sea-ice concentration climate record. *Polar Res.* **2014**, *33*, 21004. [[CrossRef](#)]
39. Ivanova, N.; Pedersen, L.T.; Tonboe, R.T.; Kern, S.; Heygster, G.; Lavergne, T.; Sørensen, A.; Saldo, R.; Dybkjær, G.; Brucker, L.; et al. Inter-comparison and evaluation of sea ice algorithms: Towards further identification of challenges and optimal approach using passive microwave observations. *Cryosphere* **2015**, *9*, 1797–1817. [[CrossRef](#)]
40. Kern, S.; Lavergne, T.; Notz, D.; Pedersen, L.T.; Tonboe, R. Satellite passive microwave sea-ice concentration data set inter-comparison for Arctic summer conditions. *Cryosphere* **2020**, *14*, 2469–2493. [[CrossRef](#)]
41. Comiso, J.C.; Cavalieri, D.J.; Parkinson, C.L.; Gloersen, P. Passive microwave algorithms for sea ice concentration: A comparison of two techniques. *Remote Sens. Environ.* **1997**, *60*, 357–384. [[CrossRef](#)]
42. Schutz, B.E.; Zwally, H.J.; Shuman, C.A.; Hancock, D.; DiMarzio, J.P. Overview of the ICESat Mission. *Geophys. Res. Lett.* **2005**, *32*, L21S01. [[CrossRef](#)]
43. Markus, T.; Neumann, T.; Martino, A.; Abdalati, W.; Brunt, K.; Csatho, B.; Farrell, S.; Fricker, H.; Gardner, A.; Harding, D.; et al. The Ice, Cloud, and Land Elevation Satellite-2 (ICESat-2): Science Requirements, Concept, and Implementation. *Remote Sens. Environ.* **2017**, *190*, 260–273. [[CrossRef](#)]
44. Ricker, R.; Hendricks, S.; Kaleschke, L.; Tian-Kunze, X.; King, J.; Haas, C. A Weekly Arctic Sea-Ice Thickness Data Record from Merged CryoSat-2 and SMOS Satellite Data. *Cryosphere* **2017**, *11*, 1607–1623. [[CrossRef](#)]
45. Yan, Q.; Huang, W. Sea Ice Thickness Measurement Using Spaceborne GNSS-R: First Results with TechDemoSat-1 Data. *IEEE J. Sel. Top. Appl. Earth Obs. Remote Sens.* **2020**, *13*, 577–587. [[CrossRef](#)]
46. Zhang, J.; Rothrock, D.A. Modeling Global Sea Ice with a Thickness and Enthalpy Distribution Model in Generalized Curvilinear Coordinates. *Mon. Weather Rev.* **2003**, *131*, 845–861. [[CrossRef](#)]
47. Taylor, K.E. Summarizing multiple aspects of model performance in a single diagram. *J. Geophys. Res. Atmos.* **2001**, *106*, 7183–7192. [[CrossRef](#)]
48. Zhang, Y.; Song, M.; Dong, C.; Liu, J. Modeling turbulent heat fluxes over Arctic sea ice using a maximum-entropy-production approach. *Adv. Clim. Change Res.* **2021**, *12*, 517–526. [[CrossRef](#)]
49. Yu, L.; Liu, J.; Gao, Y.; Shu, Q. A Sensitivity Study of Arctic Ice-Ocean Heat Exchange to the Three-Equation Boundary Condition Parametrization in CICE6. *Adv. Atmos. Sci.* **2022**, *39*, 1398–1416. [[CrossRef](#)]
50. Zhang, X. Sensitivity of Arctic Summer Sea Ice Coverage to Global Warming Forcing: Towards Reducing Uncertainty in Arctic Climate Change Projections. *Tellus A* **2010**, *62*, 220–227. [[CrossRef](#)]
51. Davy, R.; Outten, S. The Arctic Surface Climate in CMIP6: Status and Developments since CMIP5. *J. Clim.* **2020**, *33*, 8047–8068. [[CrossRef](#)]

Disclaimer/Publisher's Note: The statements, opinions and data contained in all publications are solely those of the individual author(s) and contributor(s) and not of MDPI and/or the editor(s). MDPI and/or the editor(s) disclaim responsibility for any injury to people or property resulting from any ideas, methods, instructions or products referred to in the content.